Journal of Asian Earth Sciences 257 (2023) 105830

Contents lists available at ScienceDirect

Journal of Asian Earth Sciences

journal homepage: www.elsevier.com/locate/jseaes

A conjugate fault revealed by the destructive Mw 5.6 (November 21, 2022) Cianjur earthquake, West Java, Indonesia

Pepen Supendi [a,b,*], Tom Winder [a], Nicholas Rawlinson [a], Conor Andrew Bacon [c], Kadek Hendrawan Palgunadi [d], Andrean Simanjuntak [b], Andri Kurniawan [e], Sri Widiyantoro [f,g], Andri Dian Nugraha [g], Hasbi Ash Shiddiqi [h], Ardianto [e], Daryono [b], Suko Prayitno Adi [b], Dwikorita Karnawati [b], Priyobudi [b], Gayatri Indah Marliyani [i], Iswandi Imran [j], Jajat Jatnika [b]

[a] Department of Earth Sciences – Bullard Labs, University of Cambridge, Cambridge CB30EZ, United Kingdom
[b] Agency for Meteorology, Climatology, and Geophysics, Jakarta 10720, Indonesia
[c] Lamont-Doherty Earth Observatory (LDEO), Columbia Climate School, NY 10923, USA
[d] Physical Science and Engineering, King Abdullah University of Science and Technology, Thuwal, Saudi Arabia
[e] Geophysical Engineering Study Program, Faculty of Mining and Petroleum Engineering, Institut Teknologi Bandung, Bandung 40132, Indonesia
[f] Faculty of Engineering, Maranatha Christian University, Bandung 40164, Indonesia
[g] Global Geophysics Research Group, Faculty of Mining and Petroleum Engineering, Institut Thknologi Bandung, Bandung 40132, Indonesia
[h] Department of Earth Science, University of Bergen, Allègaten 41, 5007, Bergen, Norway
[i] Geological Engineering Department, Gadjah Mada University, Yogyakarta 55281, Indonesia
[j] Structural Engineering Research Group, Faculty of Civil and Environmental Engineering, Institut Teknologi Bandung, Bandung 40132, Indonesia

ARTICLE INFO

Keywords:
Earthquake
Conjugate fault
Cianjur
West Java

ABSTRACT

On 21 November 2022, a destructive earthquake (Mw 5.6) struck Cianjur, West Java, Indonesia, resulting in at least 321 deaths, damage to 47,000 buildings, and economic losses of up to 7.7 trillion Indonesian Rupiahs (~US $546 million). Prior to this earthquake, the fault on which slip occurred had not been mapped, thus making further analysis crucial for assessing future seismic hazard in the region. We constructed a detailed earthquake catalogue, which spanned the period from 10 days before to 48 days after the mainshock, using waveform migration and stacking, followed by relative relocation using a double-difference method. Source mechanisms for selected aftershocks were estimated using waveform inversion. Our results show three clear foreshocks preceding the mainshock, while the aftershocks reveal the presence of a conjugate fault pair trending NNW-SSE with a length of ~8 km and WSW-ENE with a length of ~5 km. Directivity analysis highlights bilateral rupture of the main shock toward N20°E and N200°E, although based on the focal mechanism solutions, it is likely that there was some slip on the conjugate fault. Analysis of the Coulomb stress change induced by the mainshock shows that areas to the NNW and WSW experienced an increase in stress, consistent with the observed aftershock pattern. The nearby fault to the south (the Rajamandala Fault) experienced an increase in stress, which likely elevates the risk of it rupturing in the future.

1. Introduction

On November 21, 2022, a destructive earthquake (Mw 5.6) occurred at 06:21 UTC near Cianjur in West Java, Indonesia (location estimates from different catalogues denoted by stars in Fig. 1a). Based on a report from the Agency for Meteorology, Climatology, and Geophysics/Badan Meteorologi, Klimatologi, dan Geofisika (BMKG), the earthquake produced strong ground motion that measured between V and VI on the MMI scale in the Cianjur area, caused severe damage to >47,000 buildings, resulted in at least 321 fatalities, and brought about economic losses of up to 7.7 trillion Indonesian Rupiahs (~US $546 million) (National Disaster Management Authority/NDMA 2022). The buildings that experienced severe damage were distributed asymmetrically, i.e., mainly in the northern reaches of the mainshock rupture (BMKG, 2023).

West Java experiences some of the most intense tectonic activity in Indonesia (Supendi et al., 2018) due to the subduction of the Indo-

* Corresponding author at: Department of Earth Sciences – Bullard Labs, University of Cambridge, Cambridge CB30EZ, United Kingdom.
E-mail address: ps900@cam.ac.uk (P. Supendi).

https://doi.org/10.1016/j.jseaes.2023.105830
Received 22 March 2023; Received in revised form 21 July 2023; Accepted 25 August 2023
Available online 26 August 2023

Australian plate beneath Eurasia, which has produced a variety of terrestrial faults, including the Baribis, Lembang, Cimandiri, and Garsela faults (Irsyam et al., 2020). The Cianjur region belongs to the volcanic Bandung Zone, with much of the area covered by young volcanic deposits from the surrounding volcanoes (van Bemmelen, 1949). Based on the National Center for Earthquake Studies of Indonesia (Pusat Studi Gempa Nasional/PuSGeN) database (Irsyam et al., 2017), the Cianjur region is traversed by the Cimandiri Fault, which extends from Pelabuhanratu Bay in Sukabumi to Padalarang in the West Bandung Regency, with a total length of about 100 km. This fault is divided into

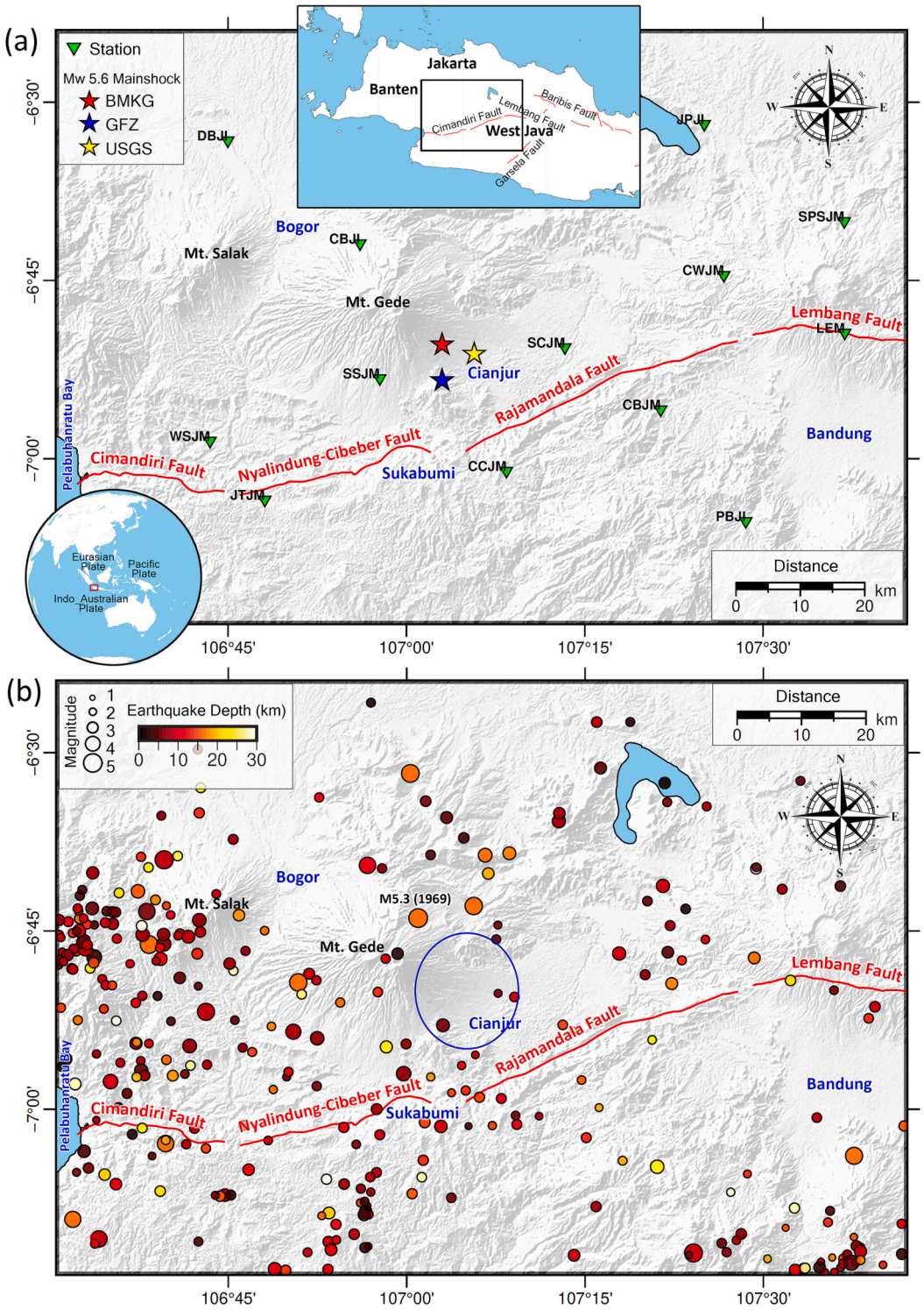

Fig. 1. (a) Epicenter estimates of the Mw 5.6 mainshock on 21 November 2022 from three different agencies are denoted by stars (red: BMKG, blue: GFZ, and yellow: USGS). Green inverted triangles depict the location of BMKG seismic stations used in this study. The lower left inset shows the location of West Java (red rectangle) with respect to Southeast Asia. The upper center inset shows the location of the study area (black rectangle) with respect to West Java. The red lines represent recognised active faults from Irsyam et al. (2017). (b) Background seismicity (depth $\leq$ 30 km) from 1963 to October 2022 according to the International Seismological Centre (ISC) and BMKG earthquake catalogue. Coloured dots denote the focal depth of the hypocenters. (For interpretation of the references to colour in this figure legend, the reader is referred to the web version of this article.)

three segments (Irsyam et al., 2017), namely the Cimandiri segment (reverse fault), the Nyalindung-Cibeber segment (reverse fault), and the Rajamandala segment (strike-slip fault) (see Fig. 1). While the behaviour of this fault is relatively well understood (Arisbaya et al., 2019; Dardji et al., 1994; Marliyani et al., 2016), the Mw 5.6 Cianjur earthquake was not located along any of its recognized segments.

Based on seismicity data from 1963 through to October 2022 (Fig. 1b), there have not been any shallow earthquakes (depth $\leq$ 30 km) with a magnitude Mw $\geq$ 5.0 in the study region in the last 60 years (see blue ellipse in Fig. 1b). The destructive earthquakes catalog in the period 1546–1950 (Martin et al., 2022) shows that the Cianjur area has experienced events of magnitude 7–8 on the 1998 European Macroseismic Scale (EMS-98) in 1834 (Raiche, 1859) and 1879 (Bergsma, 1882), respectively. However, due to limited seismic instrument coverage during the 19th century, the source fault of both earthquakes could not be meaningfully constrained. Today, the situation is very different, with BMKG operating a large national network of high-quality broadband stations that offers good coverage of the study region. This has allowed us to analyse the 2022 (Mw 5.6) Cianjur earthquake in detail, including its finite source characteristics and associated foreshock and aftershock sequences through hypocenter relocation, focal mechanism solutions, empirical Green's function, and stress changes; such an analysis will provide fresh insight into the fault responsible for the event.

2. Data and method

2.1. Earthquake location

We used continuous seismic data recorded by a permanent network of three-component broadband seismometers (Nanometrics Trillium 120Q seismometers with a flat response between 120 s and 150 Hz, coupled with Trident Digitisers that use a sample rate of 40 Hz) - see the green inverted triangles in Fig. 1a) - operated by BMKG in West Java between 10 November 2022 and 8 January 2023. From the continuous waveform data, earthquakes were automatically detected and located, and local earthquake magnitudes calculated using QuakeMigrate (Winder et al., 2021, 2022) (see example in Supplementary Fig. S1) in the presence of a one-dimensional velocity model from Koulakov et al. (2007). QuakeMigrate comprises three steps (Bacon, 2021; Winder, 2021): (1) continuous data are first transformed to onset functions via the short-term average to long-term average ratio (STA/LTA) of the signal amplitude, which are designed to peak in the neighbourhood of a seismic phase arrival, (2) these onset functions are then continuously migrated into a 3-D subsurface grid and stacked, where each grid point represents a potential hypocenter location, and each timestamp a candidate earthquake origin time, (3) peaks in the stacked function are then identified through space and time. The final output is a catalogue of event origin times and locations, corresponding to the timing and location of peaks in the maximum coalescence value, i.e., a measure of the coherence of a stack of STA/LTA functions (see Drew et al., 2013) that exceed the trigger threshold. We calculate local magnitude (M_L) following the approach of Keir et al. (2006), which is integrated into the QuakeMigrate package. Event hypocenters, origin times, and picks from QuakeMigrate were then used to refine the initial 1-D P-velocity model (Vp) via the VELEST program (Kissling et al., 1994), which performs a coupled velocity-hypocenter inversion (Supplementary Fig. S2). Due to the limited number and quality of S-wave arrival times extracted by QuakeMigrate, we did not try and invert for a 1-D S-wave velocity model (Vs). This improved 1-D velocity model was used for all subsequent analyses, with the equation from Brocher (2005) used to empirically derive an equivalent S-wave model.

2.2. Earthquake relocation

We refined the hypocenter locations using the double-difference method (Waldhauser and Ellsworth, 2000) implemented in the HypoDD program (Waldhauser, 2001). This is achieved by minimising the residuals of the differences between theoretical and observed traveltimes (extracted by QuakeMigrate) for nearby earthquake pairs recorded at each station, under the assumption that nearby sources have almost identical ray paths and traveltimes if the receiver is sufficiently distant. The maximum hypocentral separation is set to 15 km, the maximum number of neighbours per event to 20, and the minimum number of links required to define neighbours to 8. We set a maximum distance of 120 km between cluster centroid and station. Extensive testing using a range of input parameter values was undertaken to ensure that the optimal values were chosen; for example, we tested the relocation using a maximum hypocentral separation of 10 km and 5 km, and found that in both cases this increased the number of weakly linked events (10% and 21%) and outliers (7% and 8%), although the final distribution of hypocenters was similar to that obtained with our preferred parameter values. Our chosen value of 15 km as the maximum hypocentral separation is still less than the distance between event pairs and stations but decreases the proportion of weakly linked events to 7% and the proportion of outliers to 6%. We used a statistical resampling scheme based on the "bootstrap" method (Billings, 1994) to assess the location uncertainty for all relocated events. We used the final hypocenters to draw a random sample (with replacement) from the full set of observed residuals and used that sample to replace each measurement. The re-sampled dataset was then used to re-locate the events, and the resultant shifts in location were examined. This entire process was repeated 200 times, thus allowing for the estimation of 95% confidence ellipsoids for each event.

2.3. Focal mechanisms

Source mechanisms for the mainshock and selected aftershocks were determined using the stochastic Bayesian moment tensor inversion method described by Heimann et al. (2018), which requires several thousand trial models to be evaluated during the optimization. This probabilistic waveform inversion method provides a reliable means of assessing the non-double couple components of the focal mechanism. Moreover, an adaptive station weighting was applied simultaneously for individual stations due to varying site responses. The weighting factor can be derived by the inversion of mean signal amplitudes of the synthetic waveforms based on the data error statistics. The seismic moment and centroid parameters can be simultaneously determined by fitting full displacement waveforms. This method has been successfully applied in different regions (e.g., Kühn et al., 2020; Dost et al., 2020) and appears robust. We applied a bandpass filter of 0.02 and 0.08 Hz prior to implementing the technique, which is similar to the range used in other studies (Cesca et al., 2010; Tassara et al., 2022).

2.4. Apparent source time functions

The distribution of damaged and destroyed buildings, which were mainly concentrated in the northern part of the mainshock region (BMKG 2023), suggests asymmetry of rupture propagation. Several studies have applied apparent source time function (ASTFs) analysis to corroborate the azimuthal dependence of moment release rate (e.g., Cesca et al., 2011; López-Comino et al., 2012). Moreover, the focal mechanism of the mainshock reveals a relatively significant non-double couple component (~12%, see Table S1), which may be one indication that rupture occurred on multiple fault planes. By exploiting our dense station distribution, we extracted ASTFs from the mainshock waveforms that were deconvolved with the empirical Green's function of an aftershock sharing the same focal mechanism (Aftershock 7 (Table S1), rotation angle 1°) and located relatively close to the mainshock (a distance of ~ 2 km). Deconvolution was applied using multitaper spectral analysis (Prieto, 2022) with the spectral division stabilized by adding a water level parameter to the denominator. We set the water level to 0.01, the number of bandwidths to 4, and the number of tapers to 6,

since these values provided stable results. We only exploit the P-wave in the deconvolution, after applying a bandpass filter in the range 0.01–1 Hz. The S-phase is not used in our analysis because it often contains later-arriving P-wave energy and is hard to separate from the arrival of surface waves. We used north, east, and vertical component traces rather than rotations into radial and transverse components in order to have P-wave energy on all components (Cesca et al., 2011). Finally, all ASTFs from the three components were stacked.

2.5. Line source directivity analysis

We used the inferred ASTF durations to estimate finite source parameters associated with line sources following the Haskell model (Haskell, 1964). Rupture directivity is quantified by comparing ASTF duration to theoretical derivations assuming a one dimensional line source, as shown by equation (1) (Cesca et al., 2011):

$$\tau(\phi) = max\left\{ t_{r/R} + 1 - V_{R/P} cos(\phi - \alpha), t_{r/R} + \frac{L_2}{L_1} + \frac{L_2}{L_1} cos(\phi - \alpha) \right\} \quad (1)$$

where L_1 and L_2 ($L_2 \geq L_1$) is $(1-\chi)L$ and χL, respectively. χ is the ratio between the shortest and longest segments of the fault ($\chi = 0$, for unilateral rupture; $\chi = 0.5$, for bilateral rupture) and L is the total fault length. $t_{r/R}$ is the ratio between rise and rupture time, $V_{R/P}$ is the ratio between rupture speed and P-wave velocity, ϕ denotes azimuth from north, and α is directivity azimuth. In this study, we considered ranges of parameters such as $t_{r/R} = 0.2-0.6$, $V_{R/P} = 0.4-0.8$, $L = 5-10$ km, $\chi = 0-0.5$, and $\alpha = -90^{\circ}-90^{\circ}$. Estimates of each parameter are obtained by using a grid search method, as also applied in López-Comino et al. (2012).

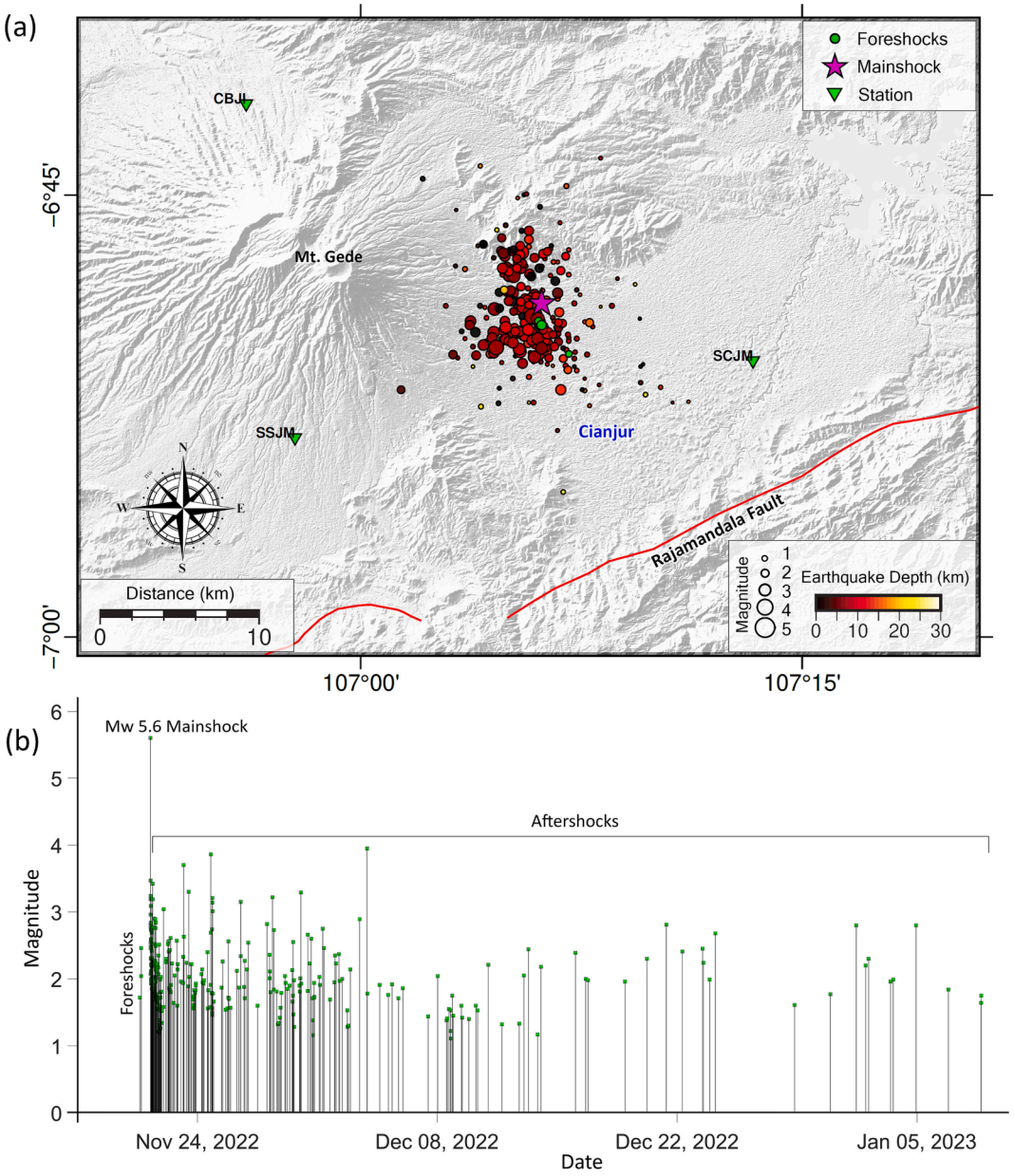

Fig. 2. (a) Initial location from QuakeMigrate after manual review, revealing a total of 283 events. The green dots indicate foreshocks (which are not colour-coded by depth), the magenta star denotes the Mw 5.6 mainshock, and the red to yellow dots indicate aftershocks colored by depth. (b) Plot showing magnitude vs time for the Mw 5.6 mainshock and associated foreshocks and aftershocks. (For interpretation of the references to colour in this figure legend, the reader is referred to the web version of this article.)

2.6. Static stress change

The geometry and degree of slip on the fault were determined by jointly considering the distribution of aftershocks and the focal mechanisms computed in the previous section. This information was then used to determine the static Coulomb stress (King et al., 1994) caused by the co-seismic slip of the mainshock through application of Coulomb 3.3 (Toda et al., 2011). The subsurface ruptures (length = 4.6 km, width = 2.7 km, and slip = 0.25 m for cluster 1; length = 8 km, width = 2.5 km, and slip = 0.25 m for cluster 2) were defined using the empirical equation from Wells and Coppersmith (1994). The static stress change associated with the strike-slip source faults were calculated at 6 km depth as implemented in the equations of Okada (1992), assuming an elastic half-space, a Poisson ratio of 0.25, and a coefficient of friction of 0.4 (Song et al., 2018). Four separate scenarios were tested, each corresponding to a different receiver fault on which future ruptures may occur.

3. Results and discussion

A total of 305 events were detected and located by QuakeMigrate within the study area (e.g., Fig. S1), extending down to ~ 20 km depth below sea level, between 20 November 2022 and 8 January 2023. Of these, 282 events were retained following manual review, including three foreshocks (M_L 1.7 – 2.5) on 20 November 2022, the mainshock on 21 November 2022, and 279 aftershocks (M_L 1.1 – 4.0) between 21 November 2022 and 8 January 2023 (Fig. 2). The average uncertainty of all located events in the E-W, N-S, and depth directions are 1.9 km, 3.1 km, and 4.5 km respectively (Fig. S2). These uncertainties are estimated within QuakeMigrate by locally fitting a 3-D Gaussian function to the marginalised coalescence map, after applying modest Gaussian smoothing. The horizontal location uncertainty is largest in the N-S direction, which is unsurprising considering the lack of stations in the north. Nevertheless, it is the uncertainty in depth that is still dominant. Poorly constrained events were removed prior to relocation using the following criteria: each event needs to have (1) at least 8P- and S-phase arrival times, and (2) an azimuthal gap no>210°. A total of 216 events passed the selection process. In total, we relocated three foreshocks, the mainshock, and 196 aftershocks related to the 2022 Cianjur earthquake (the remaining 16 events were located above the surface, and were therefore discarded). A comparison of the initial and relocated hypocentral locations are shown in Fig. S4, in both map and cross-section view. The choice of velocity model used in HypoDD can influence the relative location of hypocenters, so we have tested our location results against those obtained using an identical workflow but with the 1-D S-wave reference model of Rosalia et al. (2012), which was first converted to a P-wave model by using the empirical equation from Brocher (2005). The results (see Fig. S4) reveal a near-identical pattern of events in terms of epicentral locations, but with some differences in the depth locations, although not of sufficient magnitude to alter our interpretation. This suggests that our results are robust, but as expected the uncertainties in depth are greater than in the horizontal dimensions.

In a separate analysis of location robustness, a bootstrap analysis method is applied to obtain quantitative estimates of location uncertainty in the presence of our preferred 1-D reference model obtained from Velest. The results, which are more robust in a relative rather than absolute sense, show that mean horizontal and vertical location errors are typically less than 2 km (represented by the semimajor axis of the ellipsoid), and the corresponding maximum mislocations are less than 7 km (Fig. S5). Due to limited station coverage in the region to the north of the study area (Fig. 1), the magnitude of the horizontal location uncertainty is larger in the N-S direction compared to the E-W direction, although depth uncertainty is still greater.

Our computed moment tensor solutions are nearly 90% double-couple on average (see Table S1). The Mw 5.6 mainshock and selected aftershocks (M > 3) consistently reveal strike-slip faults with the nodal planes oriented in the NNW-SSE and WSW-ENE directions (Fig. 3). The pattern of relocated hypocenters suggests that there may be a conjugate pair of faults trending NNW-SSE and WSW-ENE, with lengths of ~ 8 km and ~ 5 km, respectively. This is supported by Interferometric Synthetic Aperture Radar (InSAR) images (Agustan, 2022) that reveal a WSW-ENE fault during ascending orbit (11–23 November 2022), but a NNW-SSE fault during descending orbit (20 November-2 December 2022). Such conjugate fault pairs capable of generating Mw less than 6 earthquakes have, to the best of our knowledge, not previously been identified in Indonesia, but can be found in other regions that exhibit earthquakes of Mw > 6, e.g., the Mw 6.1 Ludian earthquake, China (Niu et al., 2019); the 2016 Mw 7.1 Kumamoto earthquake, Japan (Lin and Chiba, 2017); and the 2019 Ridgecrest earthquake sequence, California (Fialko and Jin, 2021).

ASTF duration shows a clear azimuthal dependence (Fig. 4a). An example showing ASTF extraction from the mainshock waveform and empirical Greens functions for station JPJI (Fig. 4d) is included in Supplementary Fig. S7. The apparent duration ranges from 1.05 to 2.15 s, with the lowest duration at N100°E and N280°E. Picks are located at the intersection of the initial and final slope with uncertainties of approximately 0.05 s. Shape and apparent duration tend to vary smoothly as a function of azimuth. We found double peaks at station JPJI, which is located at N50°E. Rupture on a simple planar fault is often characterized by a single peak on the ASTF (Prieto, 2022). Complicated ASTFs indicate heterogeneous moment release along the rupture plane and may be caused by multisegmented faults, especially for earthquakes of size Mw less than 6 (e.g., Grigoli et al., 2018; Palgunadi et al., 2020; Cho et al., 2023). We observe complicated and wide ASTFs that are not characterized by a single peak at several stations including DBJI, PTJI, WLJI, SKJI, and CSJI. Therefore, the earthquake source likely exhibits slip on multisegmented faults. Further evidence of rupture on multisegmented faults is indicated by the cross-cutting spatial distribution of aftershocks (Fig. 3). However, as shown by stacked ASTFs from all stations (Fig. S8), the heterogeneity of the source directivity is minimal, which stipulates dominant moment release on one fault plane.

Directivity analysis is undertaken by assuming a one-dimensional line source model. Based on a grid search over five parameters, we found that the best fit value in each case occurs when the (1) ratio between rise and rupture time is $(t_{r/R}) = 0.5$, (2) ratio between rupture speed and P-wave velocity is $(V_{R/P}) = 0.6$; (3) ratio between the shortest and longest segments of the fault is $L = 8$ km; (4) total fault length is $\chi = 0.5$; and (5) directivity azimuth is $(\alpha) = 20^{\circ}$ (see black line in Fig. 4b). Using a simple 1-D line source, we observed a rise time equal to half of the rupture time, which may indicate a pulse-like rupture, and a rupture speed of $0.6V_P$, which is sub-shear. The best fit model to the ASTF duration (Fig. 4b, 4c, 4d) exhibits bilateral rupture towards N20°E and N200°E. The directivity orientation is misaligned with the spatial distribution of the aftershocks (e.g., Aktar et al., 2007). However, this is likely caused by the resultant/combined slip on two conjugate faults, and therefore is to be expected. Assuming V_s= ~3.5 km/s.V_r = 0.9 × V_s= 3.15 km/s, and given that the total ASTF duration at station DBJI is 2.1 s, the rupture length should be 6.6 km (3.15 km/s × 2.1 s). The length of the WSW-ENE fault is ~ 5 km (based on the aftershock distribution), which obviously cannot accommodate this rupture and hence the NNW-SSE fault of length ~ 8 km is also required. Station DBJI is located N300°E relative to the event, almost perpendicular to the main directivity orientation. This misalignment may be explained by radiated seismic energy from co-seismic slip on two conjugate faults because 1-D line sources can only consider the combined effect of two faults. The direction of propagation of the radiated seismic energy can be approximated using simple vectorization of the two conjugate fault plane solutions of the mainshock (Table S1), along with the seismic moment ratio of the fault segments (6.5:1), extracted from Figure S8. Directivity analysis using a single line source reveals bilateral rupture propagation oriented at N20°E and N200°E, which is consistent with a moment ratio

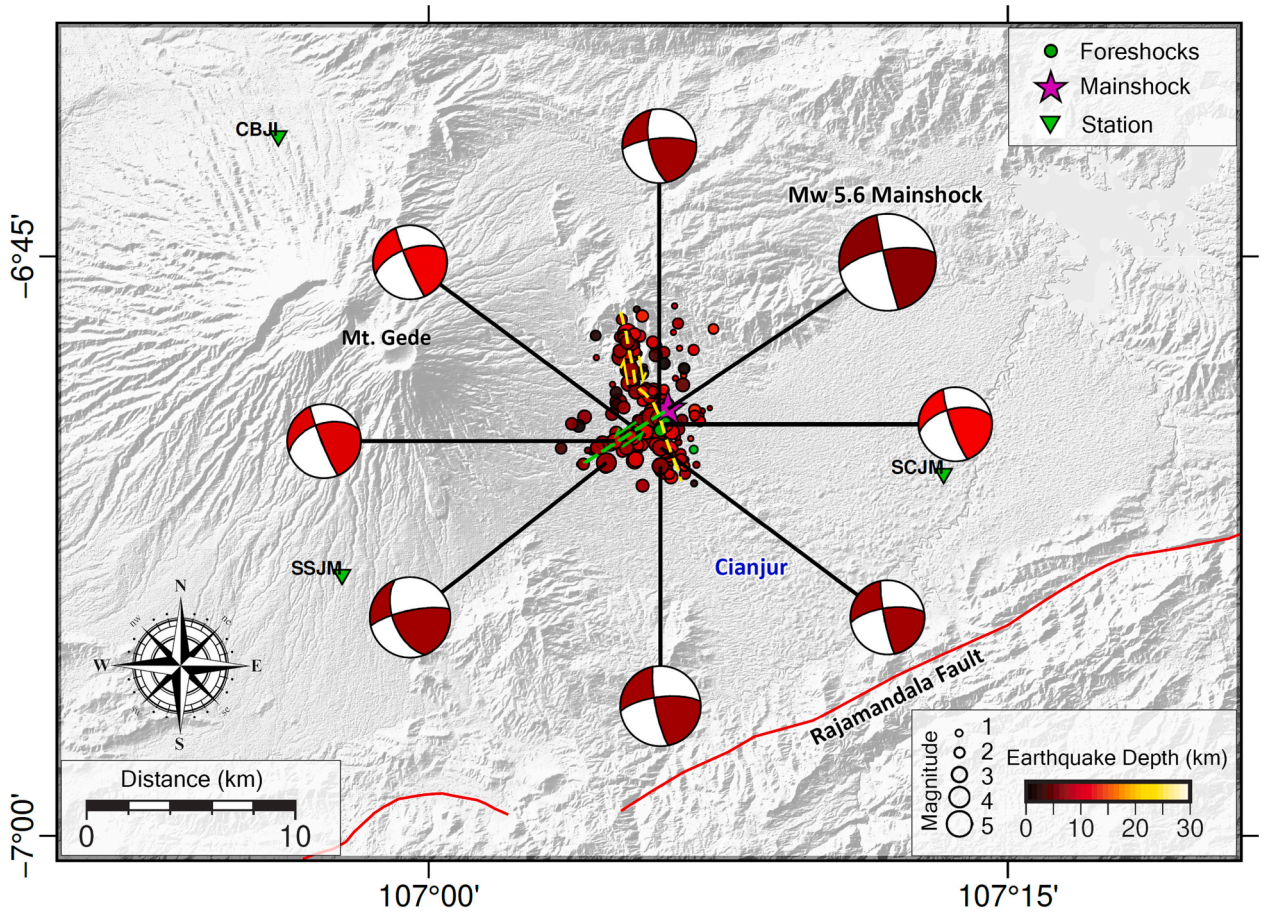

Fig. 3. Map view of relocated events and focal mechanism solutions for the foreshocks (green dots), Mw 5.6 mainshock (magenta star), and associated aftershocks (red dots). Note that foreshocks are not colour-coded by depth. The dashed yellow and green lines denote the approximate location and sense of movement along the faults, based on the aftershock distribution and focal mechanisms. Red lines correspond to major crustal faults in the region extracted from Irsyam et al. (2017). Green inverted triangles denote the location of BMKG seismic stations closest to the events. (For interpretation of the references to colour in this figure legend, the reader is referred to the web version of this article.)

of 6.5:1 between the NNW-SSE and WSW-ENE segments. This directivity observation may explain extensive building destruction along the NS fault segment (BMKG, 2023). However, a more extensive analysis of earthquake source characteristics should be carried out to confirm the directivity (e.g., finite fault inversion, stress drop, and radiated seismic energy).

The Coulomb stress change has the potential to explain the aftershock distribution and provide insight into the possible locations of future earthquakes (King et al., 1994; Stein and Lisowski, 1983). Static stress changes caused by the Mw 5.6 mainshock (Fig. 5) reveal areas of increased stress (depicted in red in Fig. 5a, b and c) in the near-field region (~ less than 10 km) to the NNW, ENE, SSE and WSW relative to the mainshock. The areas that experienced stress drops (depicted in blue) are at greater distances (~ > 10 km) from the mainshock to the NNE, ESE, SSW, and WNW. It is likely that the mainshock energy release immediately reduced stress at the rupture location; this stress then transferred to the NNW and WSW and caused aftershocks, since these areas exhibit high static Coulomb stress changes. Importantly, the high static Coulomb stress transfer to the SSE of the mainshock (Fig. 5c) requires further investigation, since it has the potential to trigger a rupture of the nearby (strike-slip) Rajamandala Fault, particularly if it is critically stressed or close to failure. Given that the Rajamandala Fault is close to many population centers, even a moderate earthquake along this fault may pose significant hazard to the region.

Based on the Peak Ground Acceleration (PGA) map at bedrock (with Vs between 750 and 1500 m/s) for 2% probability of exceedance in 50 years (Irsyam et al., 2020), the Cianjur region has a modeled PGA value of less than 1 g. The geological map from Sudjatmiko (1972) shows that the damaged areas are located on young volcanic products, for which BMKG reported a maximum PGA of around 0.5 g for the Mw 5.6 earthquake. Although this is well within the PGA estimates of the hazard model, the fact that many houses and buildings were damaged demonstrates that they were not suitably constructed or retrofitted to withstand expected ground accelerations. Destructive earthquakes have struck in this area in the past (1834 and 1879), in addition to the late 2022 event that is the focus of this study. Therefore, spatial and regional planning should consider retrofitting buildings to withstand ground motion of at least 0.5 g; it is evident from the destruction that many buildings don't come close to being able to take PGAs estimated by current hazard maps (it may be that many were constructed before the maps existed), so clearly any new builds need to be considerably more resilient to ground motion than pre-existing structures.

4. Conclusion

The Mw 5.6 Cianjur earthquake and associated aftershocks were caused by slip along a newly identified conjugate strike-slip fault system, comprised of two segments trending NNW-SSE and WSW-ENE, with lengths of ~ 8 km and ~ 5 km, respectively. The mainshock was preceded by three foreshocks on the previous day and 196 aftershocks up until January 8th 2023. The mainshock increased stress to the NNW and WSW based on an assessment of the Coulomb stress change, which

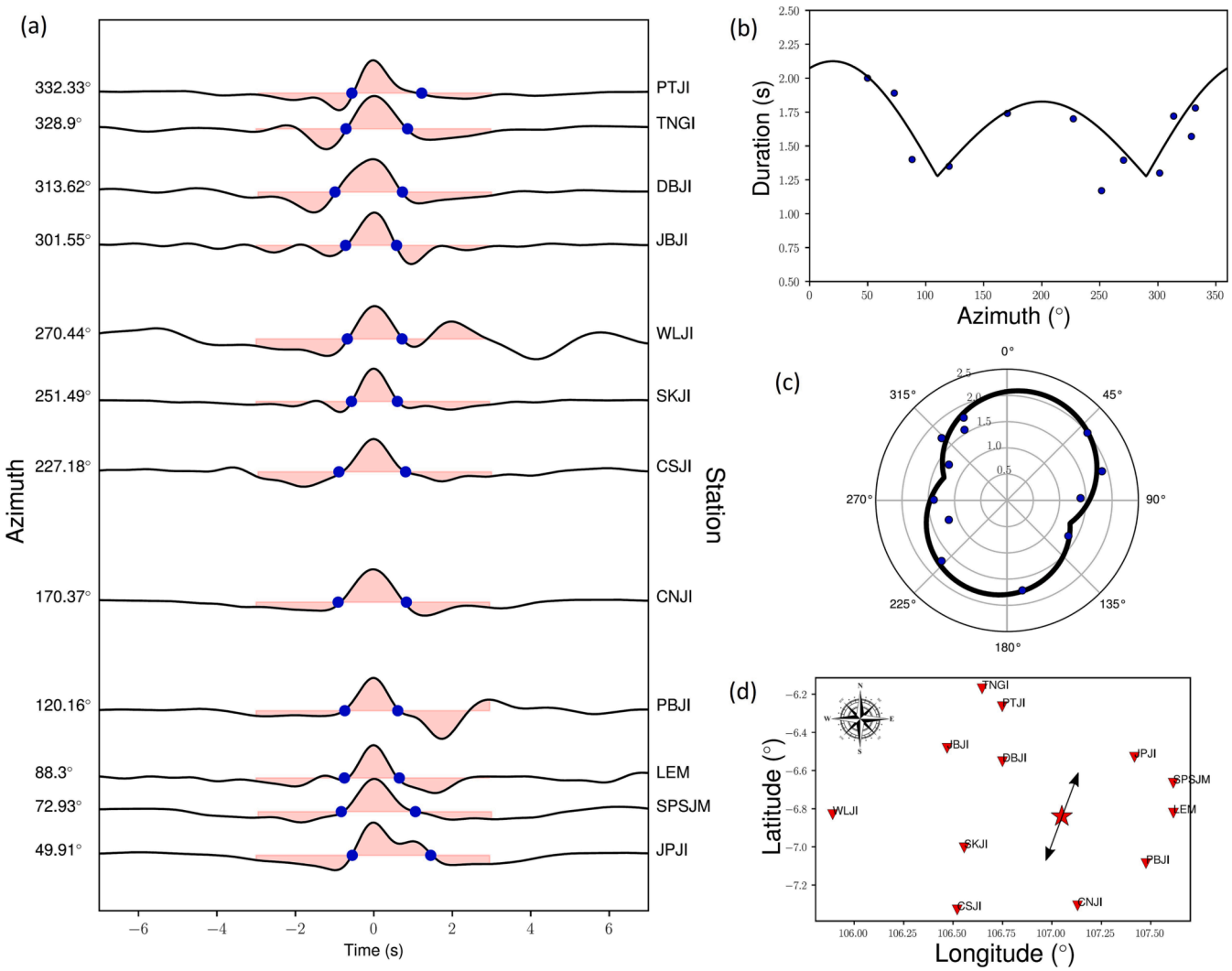

Fig. 4. Directivity analysis assuming a point source and using a one-dimensional Haskell line source model. (a) Apparent source time functions (ASTFs) obtained from the deconvolution of an aftershock P-wave from the mainshock P-wave. ASTFs are arranged by azimuth from north. Manual picking of onset and offset of the ASTFs are shown by blue dots. (b) ASTF durations (blue dots) versus azimuth and theoretical prediction (black line) for the best fitting line source of a bilateral rupture. (c) Polar plot of ASTF duration (blue dots) and the theoretical estimate (black line) showing bilateral rupture toward N20°E and N200°E. (d) Stations used for directivity analysis. Black arrows denote bilateral rupture toward N20°E and N200°E. (For interpretation of the references to colour in this figure legend, the reader is referred to the web version of this article.)

coincides with the distribution of aftershocks in this area. Critically, this sequence has also generated high Coulomb stress changes to the SSE, which may have implications for the likelihood of a large earthquake occurring on the Rajamandala Fault.

5. Availability of data and materials

Earthquake data are available at https://doi.org/10.5281/zenodo.7600097. All figures were made using the Generic Mapping Tools version 6 (Wessel et al., 2019). Topography data were sourced from the Digital Elevation Model Nasional (https://tanahair.indonesia.go.id/demnas). Waveform data were taken from https://geof.bmkg.go.id/webdc3 with permission from BMKG. QuakeMigrate software was sourced from https://doi.org/10.5281/zenodo.4442749.

Funding

This study is funded by the University of Cambridge through a Herchel Smith Research Fellowship awarded to P.S., British Council grant G107511 awarded to N. R., Research Center for Disaster Mitigation (PPMB) ITB awarded to S.W., and was supported by Konsorsium Gempabumi dan Tsunami BMKG.

7. Authors' contributions

P.S., N.R., C.A.B., K.H.P., and S.W. wrote the manuscript; P.S. performed the hypocenter location and relocation together with T.W. and C.A.B; A.S. performed the focal mechanism analysis, KHP performed the directivity analysis; A.K. performed the coulomb static stress analysis. All authors have reviewed and contributed to the preparation of the manuscript.

CRediT authorship contribution statement

Pepen Supendi: Conceptualization, Methodology, Writing – original draft, Writing – review & editing, Visualization, Formal analysis. **Tom Winder:** Methodology, Software, Writing – original draft. **Nicholas Rawlinson:** Writing – review & editing, Supervision, Formal analysis, Funding acquisition. **Conor Andrew Bacon:** Writing – review & editing, Supervision, Formal analysis, Funding acquisition. **Kadek Hendrawan**

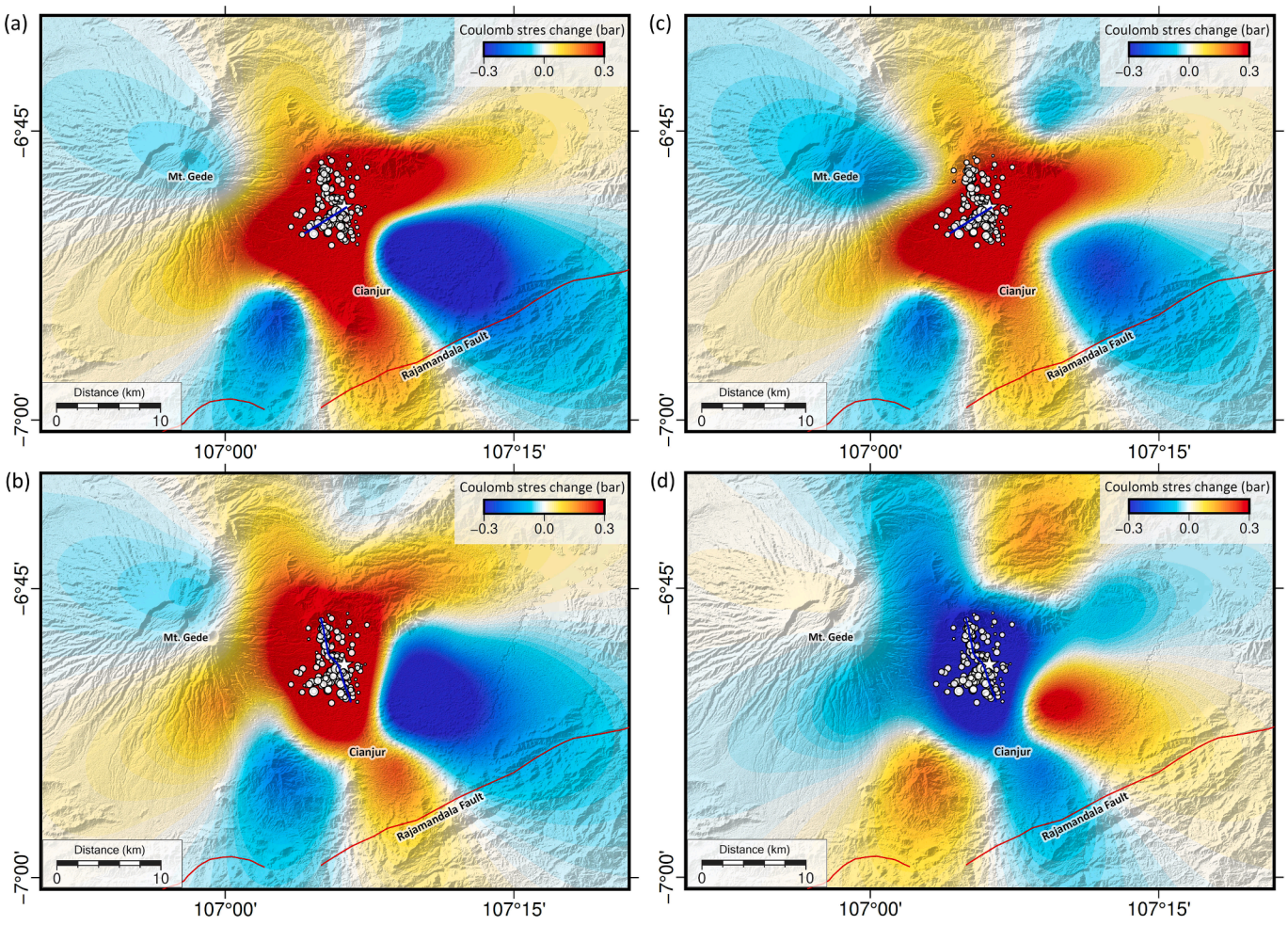

Fig. 5. Modeled Coulomb stress change for four different receiver faults (a) strike-slip fault corresponding to WSW-ENE fault; (b) strike-slip fault corresponding to NNW-SSE fault; (c) strike-slip fault corresponding to the Rajamandala Fault; (d) strike-slip fault corresponding to the Rajamandala Fault. The blue line in each plot denotes the source fault, which corresponds to either the NNW-SSE fault or its conjugate pair. (For interpretation of the references to colour in this figure legend, the reader is referred to the web version of this article.)

Palgunadi: Methodology, Writing – original draft, Formal analysis. **Andrean Simanjuntak:** Methodology, Writing – original draft. **Andri Kurniawan:** Supervision. **Sri Widiyantoro:** . **Andri Dian Nugraha:** . **Hasbi Ash Shiddiqi:** Methodology. **Ardianto:** Methodology. **Daryono:** Resources. **Suko Prayitno Adi:** Resources. **Dwikorita Karnawati:** Resources. **Priyobudi:** Resources. **Gayatri Indah Marliyani:** Formal analysis. **Iswandi Imran:** Resources. **Jajat Jatnika:** Resources.

Declaration of Competing Interest

The authors declare that they have no known competing financial interests or personal relationships that could have appeared to influence the work reported in this paper.

Data availability

Data will be made available on request.

Acknowledgements

We thank the Agency for Meteorology, Climatology, and Geophysics (BMKG) of Indonesia for granting access to the earthquake data used in this research.

Appendix A. Supplementary data

Supplementary data to this article can be found online at https://doi.org/10.1016/j.jseaes.2023.105830.

References

Agustan,, 2022. Deformasi Permukaan terkait Gempa Cianjur Mw 5.9 21 November 2022 berbasis Interferometric Synthetic Aperture Radar (InSAR). National Research and Innovation Agency, Indonesia.

Aktar, M., Karabulut, H., Özalaybey, S., Childs, D., 2007. A conjugate strike-slip fault system within the extensional tectonics of Western Turkey. Geophysical Journal International 171, 1363–1375. https://doi.org/10.1111/j.1365-246X.2007.03598.x.

Arisbaya, I., Handayani, L., Mukti, M.M., Sudrajat, Y., Grandis, H., Sumintadireja, P., 2019. Imaging the Geometry of Cimandiri Fault Zone Based on 2D Audio-Magnetotelluric (AMT) Model in Nyalindung, Sukabumi-Indonesia. Pure Appl. Geophys. 176, 4833–4845. https://doi.org/10.1007/s00024-019-02241-0.

Bacon, C., 2021. Seismic anisotropy and microseismicity: from crustal formation to subduction termination. https://doi.org/10.17863/CAM.82196.

Bergsma, P.A., 1882. Uitbarstingen van vulkanen en aardbevingen in den Oost Indischen Archipel waargenomen gedurende het jaar 1879. Natuurkundig tijdschrift voor Nederlandsch Indië 41, 49–57.

Billings, S.D., 1994. Simulated annealing for earthquake location. Geophysical Journal International 118, 680–692. https://doi.org/10.1111/j.1365-246X.1994.tb03993.x.

Bmkg, 2023. Peta Bahaya Gempabumi Cianjur (dengan Sumber Gempa Patahan Cugenang). Accessed: 25 January 2023. https://www.bmkg.go.id/berita/?p=peta-bahaya-gempabumi-cianjur-dengan-sumber-gempa-patahan-cugenang&lang=ID.

Brocher, T.M., 2005. Empirical Relations between Elastic Wavespeeds and Density in the Earth's Crust. Bulletin of the Seismological Society of America 95, 2081–2092. https://doi.org/10.1785/0120050077.

Cesca, S., Heimann, S., Stammler, K., Dahm, T., 2010. Automated procedure for point and kinematic source inversion at regional distances. Journal of Geophysical Research 115, B06304. https://doi.org/10.1029/2009JB006450.

Cesca, S., Heimann, S., Dahm, T., 2011. Rapid directivity detection by azimuthal amplitude spectra inversion. Journal of Seismology 15, 147–164. https://doi.org/10.1007/s10950-010-9217-4.

Cho, E., Woo, J.-U., Rhie, J., Kang, T.-S., Baag, S.-Y., 2023. Rupture Process of the 2017 Mw 5.5 Pohang, South Korea, Earthquake via an Empirical Green's Function Method. Bulletin of the Seismological Society of America. Doi: 10.1785/0120220161.

Dardji, N., Villemin, T., Rampnoux, J.P., 1994. Paleostresses and strike-slip movement: the Cimandiri Fault Zone, West Java, Indonesia. Journal of Southeast Asian Earth Sciences 9, 3–11. https://doi.org/10.1016/0743-9547(94)90061-2.

Dost, B., van Stiphout, A., Kühn, D., Kortekaas, M., Ruigrok, E., Heimann, S., 2020. Probabilistic Moment Tensor Inversion for Hydrocarbon-Induced Seismicity in the Groningen Gas Field, the Netherlands, Part 2: Application. Bulletin of the Seismological Society of America 110, 2112–2123. https://doi.org/10.1785/0120200076.

Drew, J., White, R.S., Tilmann, F., Tarasewicz, J., 2013. Coalescence microseismic mapping. Geophysical Journal International 195, 1773–1785. https://doi.org/10.1093/gji/ggt331.

Fialko, Y., Jin, Z., 2021. Simple shear origin of the cross-faults ruptured in the 2019 Ridgecrest earthquake sequence. Nature Geoscience 14, 513–518. https://doi.org/10.1038/s41561-021-00758-5.

Grigoli, F., Cesca, S., Rinaldi, A.P., Manconi, A., López-Comino, J.A., Clinton, J.F., Westaway, R., Cauzzi, C., Dahm, T., Wiemer, S., 2018. The November 2017 M_w 5.5 Pohang earthquake: A possible case of induced seismicity in South Korea. Science 360, 1003–1006. https://doi.org/10.1126/science.aat2010.

Haskell, N.A., 1964. Total energy and energy spectral density of elastic wave radiation from propagating faults. Bulletin of the Seismological Society of America 54, 1811–1841. https://doi.org/10.1785/BSSA05406A1811.

Heimann, S., Isken, M., Kühn, D., Sudhaus, H., Steinberg, A., Daout, S., Cesca, S., Vasyura-Bathke, H., Dahm, T., 2018. Grond - A probabilistic earthquake source inversion framework. https://doi.org/10.5880/GFZ.2.1.2018.003.

Irsyam, M., Cummins, P.R., Asrurifak, M., Faizal, L., Natawidjaja, D.H., Widiyantoro, S., Meilano, I., Triyoso, W., Rudiyanto, A., Hidayati, S., Ridwan, M., Hanifa, N.R., Syahbana, A.J., 2020. Development of the 2017 national seismic hazard maps of Indonesia. Earthquake Spectra 875529302095120. https://doi.org/10.1177/8755293020951206.

Irsyam, M., Widiyantoro, S., Natawidjaja, D.H., Meilano, I., Rudyanto, A., Hidayati, S., Triyoso, W., Hanifa, N.R., Djarwadi, D., Faizal, L., Sunarjito, S. (Eds.), 2017. Peta sumber dan bahaya gempa Indonesia tahun 2017, Cetakan pertama. ed. Pusat Penelitian dan Pengembangan Perumahan dan Permukiman, Badan Penelitian dan Pengembangan, Kementerian Pekerjaan Umum, Bandung.

Keir, D., Stuart, G.W., Jackson, A., Ayele, A., 2006. Local Earthquake Magnitude Scale and Seismicity Rate for the Ethiopian Rift. Bulletin of the Seismological Society of America 96, 2221–2230. https://doi.org/10.1785/0120060051.

King, G.C.P., Stein, R.S., Lin, J., 1994. Static stress changes and the triggering of earthquakes. Bulletin of the Seismological Society of America 84, 935–953. https://doi.org/10.1785/BSSA0840030935.

Kissling, E., Ellsworth, W.L., Eberhart-Phillips, D., Kradolfer, U., 1994. Initial reference models in local earthquake tomography. Journal of Geophysical Research 99, 19635–19646. https://doi.org/10.1029/93JB03138.

Koulakov, I., Bohm, M., Asch, G., Lühr, B.-G., Manzanares, A., Brotopuspito, K.S., Fauzi, P., Purbawinata, M.A., Puspito, N.T., Ratdomopurbo, A., Kopp, H., Rabbel, W., Shevkunova, E., 2007. P and S velocity structure of the crust and the upper mantle beneath central Java from local tomography inversion. Journal of Geophysical Research 112, B08310. https://doi.org/10.1029/2006JB004712.

Kühn, D., Heimann, S., Isken, M.P., Ruigrok, E., Dost, B., 2020. Moment tensor inversion testing report on hydrocarbon-induced seismicity in the Groningen gas field, the Netherlands. Doi: 10.5880/GFZ.2.1.2020.003.

Lin, A., Chiba, T., 2017. Coseismic conjugate faulting structures produced by the 2016 M w 7.1 Kumamoto earthquake, Japan. Journal of Structural Geology 99, 20–30. https://doi.org/10.1016/j.jsg.2017.05.003.

López-Comino, J.-Á., de Mancilla, F., L., Morales, J., Stich, D.,, 2012. Rupture directivity of the 2011, Mw 5.2 Lorca earthquake (Spain): THE 2011 LORCA EARTHQUAKE. Geophysical Research Letters 39, n/a-n/a. https://doi.org/10.1029/2011GL050498.

Marliyani, G.I., Arrowsmith, J.R., Whipple, K.X., 2016. Characterization of slow slip rate faults in humid areas: Cimandiri fault zone, Indonesia. Journal of Geophysical Research: Earth Surface 121, 2287–2308. https://doi.org/10.1002/2016JF003846.

Martin, S.S., Cummins, P.R., Meltzner, A.J., 2022. Gempa Nusantara: A Database of 7380 Macroseismic Observations for 1200 Historical Earthquakes in Indonesia from 1546 to 1950. Bulletin of the Seismological Society of America 112, 2958–2980. https://doi.org/10.1785/0120220047.

NDMA, 2022. Korban meninggal dunia pasca gempabumi Cianjur. Accessed 27 November 2022. https://www.bnpb.go.id/berita/.

Niu, Y., Wang, S., Zhu, W., Zhang, Q., Lu, Z., Zhao, C., Qu, W., 2019. The 2014 Mw 6.1 Ludian Earthquake: The Application of RADARSAT-2 SAR Interferometry and GPS for this Conjugated Ruptured Event. Remote Sensing 12, 99. https://doi.org/10.3390/rs12010099.

Okada, Y., 1992. Internal deformation due to shear and tensile faults in a half-space. Bulletin of the Seismological Society of America 82, 1018–1040. https://doi.org/10.1785/BSSA0820021018.

Palgunadi, K.H., Gabriel, A.-A., Ulrich, T., López-Comino, J.Á., Mai, P.M., 2020. Dynamic Fault Interaction during a Fluid-Injection-Induced Earthquake: The 2017 Mw 5.5 Pohang Event. Bulletin of the Seismological Society of America 110, 2328–2349. https://doi.org/10.1785/0120200106.

Prieto, G.A., 2022. The *Multitaper* Spectrum Analysis Package in Python. Seismological Research Letters 93, 1922–1929. https://doi.org/10.1785/0220210332.

Raiche, M.T., 1859. Berighten over aardbevingen en berguitbarstingen vermeld in de Javasche Couranten van 1831 to 1840. Natuurkundig tijdschrift voor Nederlandsch Indië 18, 245–282.

Rosalia, S., Widiyantoro, S., Cummins, P.R., Yudistira, T., Nugraha, A.D., Zulfakriza, Z., Setiawan, A., 2022. Upper crustal shear-wave velocity structure Beneath Western Java, Indonesia from seismic ambient noise tomography. Geosci. Lett. 9, 1. https://doi.org/10.1186/s40562-021-00208-5.

Song, G., Wang, C., Wang, B., 2018. Structural Health Monitoring (SHM) of Civil Structures. MDPI AG Illustrated edition.

Stein, R.S., Lisowski, M., 1983. The 1979 Homestead Valley Earthquake Sequence, California: Control of aftershocks and postseismic deformation. Journal of Geophysical Research 88, 6477. https://doi.org/10.1029/JB088iB08p06477.

Sudjatmiko, 1972. Geologic map of the Cianjur quadrangle.

Supendi, P., Nugraha, A.D., Puspito, N.T., Widiyantoro, S., Daryono, D., 2018. Identification of active faults in West Java, Indonesia, based on earthquake hypocenter determination, relocation, and focal mechanism analysis. Geoscience Letters 5. https://doi.org/10.1186/s40562-018-0130-y.

Tassara, C., Cesca, S., Miller, M., López-Comino, J.Á., Sippl, C., Cortés-Aranda, J., Schurr, B., 2022. Seismic source analysis of two anomalous earthquakes in Northern Chile. Journal of South American Earth Sciences 119, 103948. https://doi.org/10.1016/j.jsames.2022.103948.

Toda, S., Stein, R.S., Sevilgen, V., Lin, J., 2011. Coulomb 3.3 Graphic-rich deformation and stress-change software for earthquake, tectonic, and volcano research and teaching-user guide (Report No. 2011–1060), Open-File Report. Reston, VA. Doi: 10.3133/ofr20111060.

van Bemmelen, R.W., 1949. The geology of Indonesia. Government Printing Office, Nijhoff, The Hague.

Waldhauser, F., Ellsworth, W.L., 2000. A Double-Difference Earthquake Location Algorithm: Method and Application to the Northern Hayward Fault, California. Bulletin of the Seismological Society of America 90, 1353–1368. https://doi.org/10.1785/0120000006.

Waldhauser, F., 2001. hypoDD-A Program to Compute Double-Difference Hypocenter Locations (Report No. 2001–113). Doi: 10.3133/ofr01113.

Wells, D.L., Coppersmith, K.J., 1994. New empirical relationships among magnitude, rupture length, rupture width, rupture area, and surface displacement. Bulletin of the Seismological Society of America 84, 974–1002. https://doi.org/10.1785/BSSA0840040974.

Wessel, P., Luis, J.F., Uieda, L., Scharroo, R., Wobbe, F., Smith, W.H.F., Tian, D., 2019. The Generic Mapping Tools Version 6. Geochemistry, Geophysics, Geosystems 20, 5556–5564. https://doi.org/10.1029/2019GC008515.

Winder, T., 2021. Tectonic earthquake swarms in the Northern Volcanic Zone. Iceland. https://doi.org/10.17863/CAM.82505.

Winder, T., Bacon, C., Smith, J., Hudson, T., Greenfield, T., White, R., 2022. QuakeMigrate: a modular, open-source python package for automatic earthquake detection and location. Authorea Preprints.

Winder, T., Bacon, C., Smith, J.D., Hudson, T.S., Drew, J., White, R.S., 2021. QuakeMigrate v1.0.0. Doi: 10.5281/ZENODO.4442749.